Figure 3.3-3: Ray path through multilayered structure.

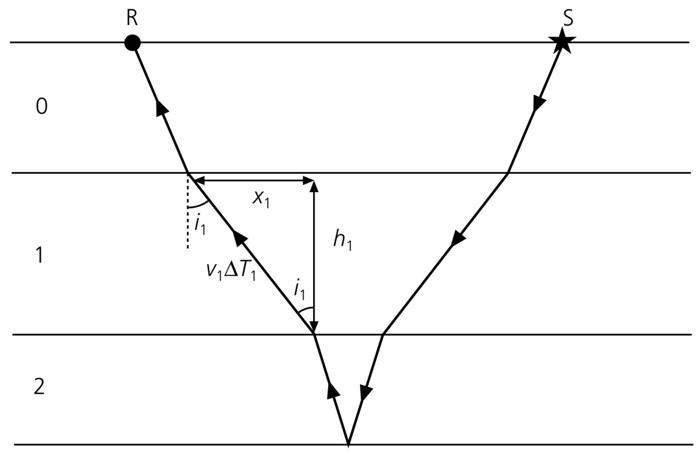

Dix equation: $\mathrm{v}_n^2 = \dfrac{\bar{\mathrm{V}}_n^2 t_n - \bar{\mathrm{V}}_{n-1}^2 t_{n-1}}{t_n - t_{n-1}}$.

where

$$\bar{\mathrm{V}}_n{}^2 = \left(\sum_{j=0}^{n} \mathrm{v}_j^2 \Delta t_j\right) \Big/ \left(\sum_{j=0}^{n} \Delta t_j\right).$$

$\bar{\mathrm{V}}_n$ is the time-weighted root mean square velocity for the first n layers.

Figure 3.3-4: Travel time curves for multiple layer reflections.

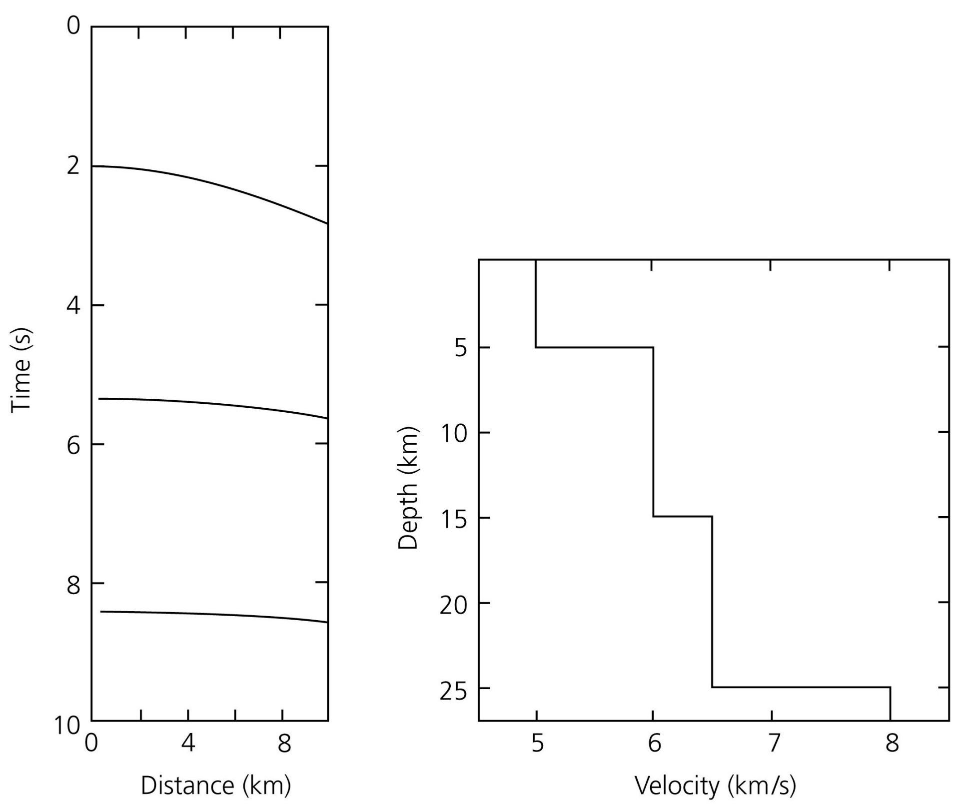

Figure 3.3-5: Travel time curve for reflections off of a dipping layer.

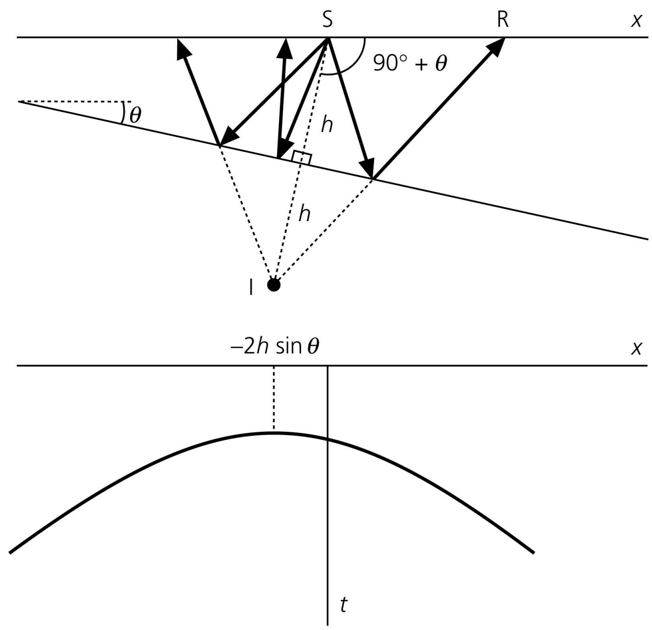

$$v_0^2 = \left[x^2 + 4h^2 - 4hx\cos(\theta + \pi/2)\right] / \ T^2$$

$$= \left[x^2 + 4h^2 + 4hx\sin\theta\right] / \ T^2$$

This travel time curve is a hyperbola with minimum at $-2h\sin\theta$, so it is not symmetric about the time axis.

Figure 3.3-6: Ray path in a medium with smoothly increasing velocities.

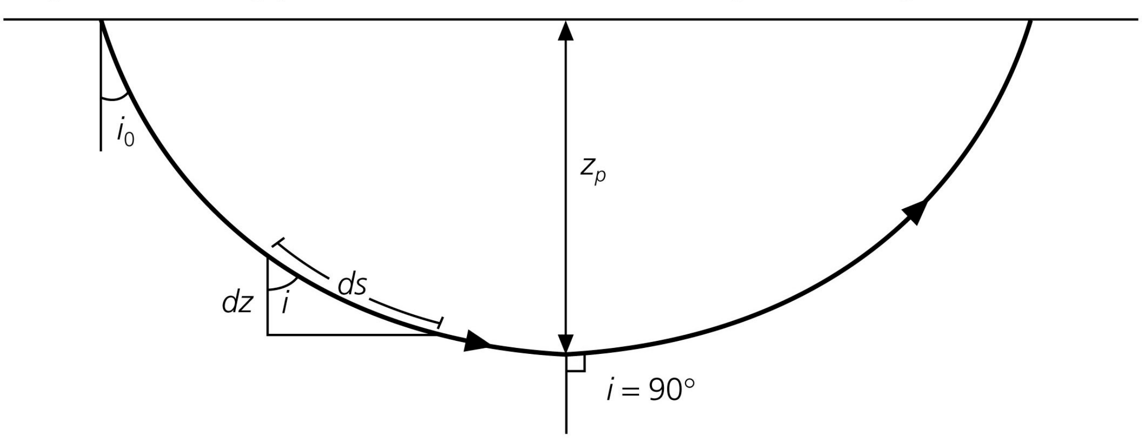

$$p = \sin i / v(z) \qquad \tan i = \frac{dx}{dz} \qquad dx = dz \tan i$$

$$x(p) = 2\int dx = 2\int_0^{z_p} \tan i \ dz = 2p\int_0^{z_p} \left(\frac{1}{v^2(z)} - p^2\right)^{-1/2} dz$$

(using $\sin i = pv(z)$ and $\cos i = (1 - \sin^2 i)^{1/2} = (1 - p^2 v^2(z))^{1/2}$)

Figure 3.3-6: Ray path in a medium with smoothly increasing velocities.

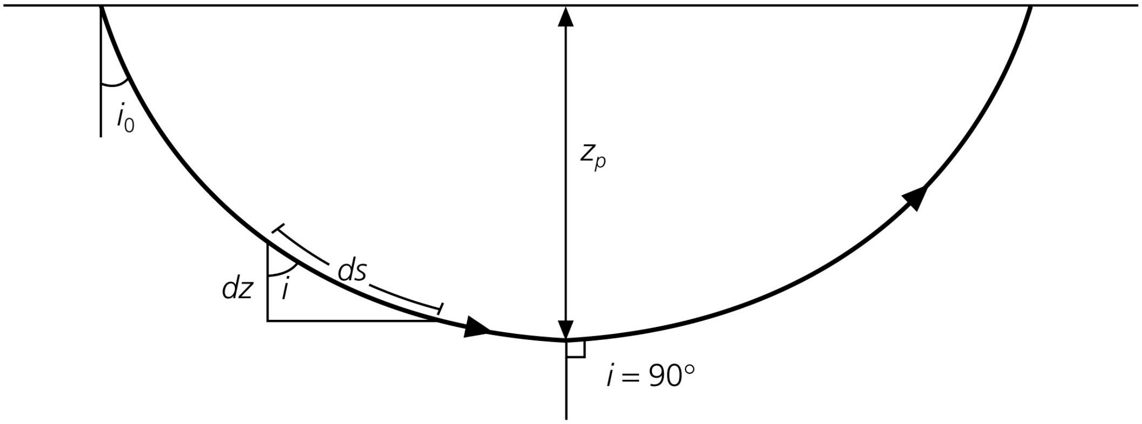

Write in terms of the slowness, $u(z) = 1/\mathrm{v}(z)$:

$$x(p) = 2p \int_0^{z_p} \frac{dz}{(u^2(z) - p^2)^{1/2}} \quad \text{and} \quad T(p) = \,= 2 \int_0^{z_p} \frac{u^2(z)dz}{(u^2(z) - p^2)^{1/2}}$$

Valid everywhere except at the exact bottom, where $u(z)$ equals p.

Figure 3.3-2: Cartoon demonstration of ray parameter.

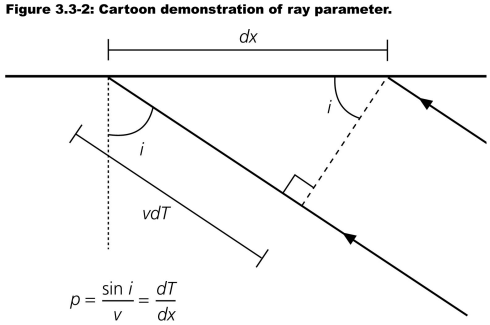

Figure 3.3-22: Velocity filtering in the frequency and wavenumber domain.

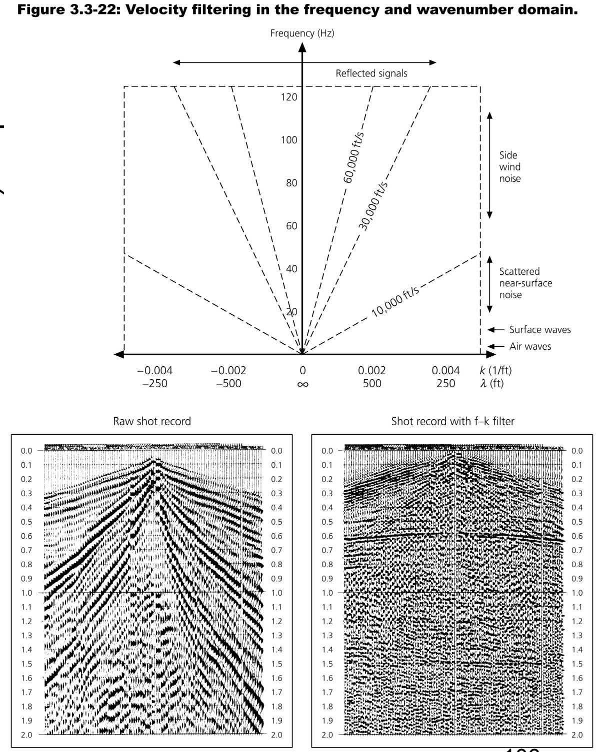

Figure 3.3-10: Cartoon geometry of a multichannel seismic reflection profile.

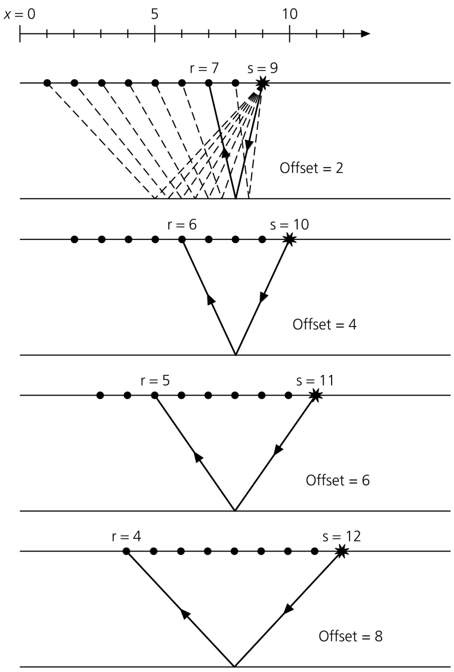

Figure 3.3-13: Cartoon of the four different gather types.

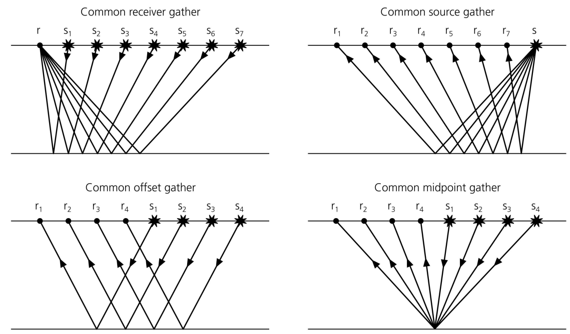

Figure 3.3-16: Cartoon of CMP stacking and velocity analysis.

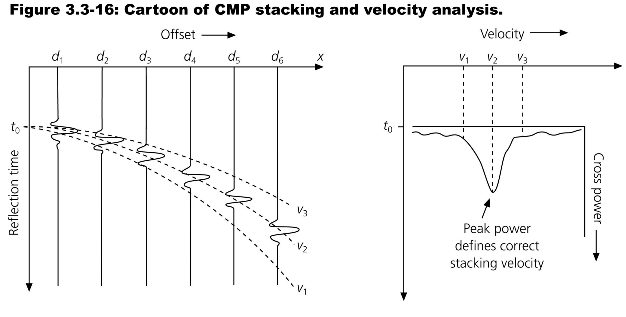

Figure 3.3-4: Travel time curves for multiple layer reflections.

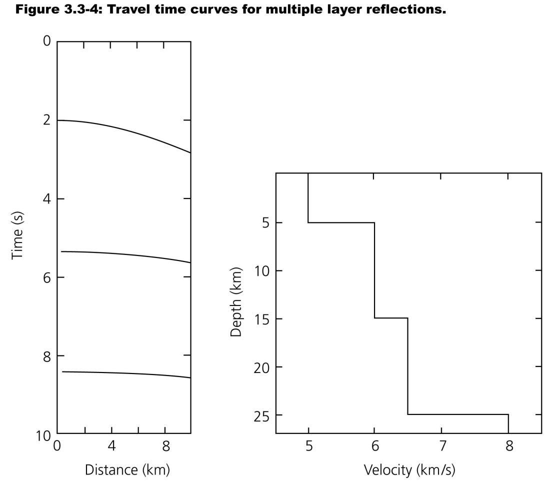

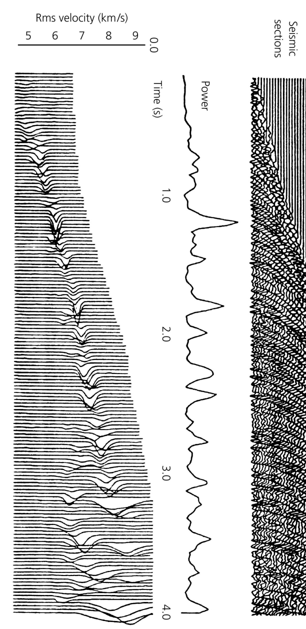

Figure 3.3-17: Example of CMP stacking and velocity analysis.

Figure 3.3-18: Illustration of forming a zero-offset section by CMP stacking.

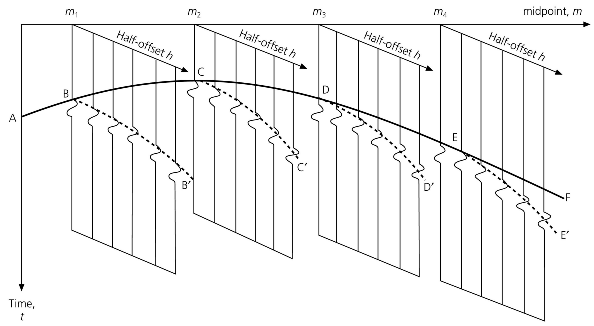

Figure 3.3-19: CMP stacking for flat and dipping layers.

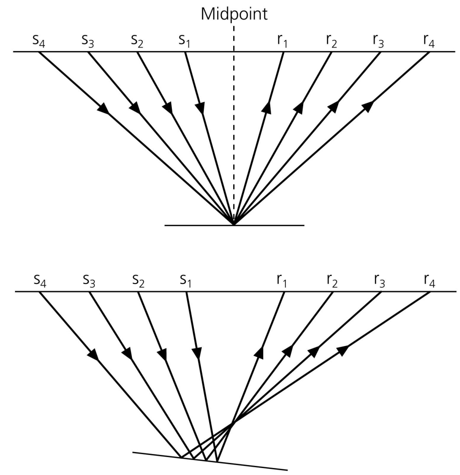

Figure 3.3-7: Relation between travel time curve, tau, and ray parameter.

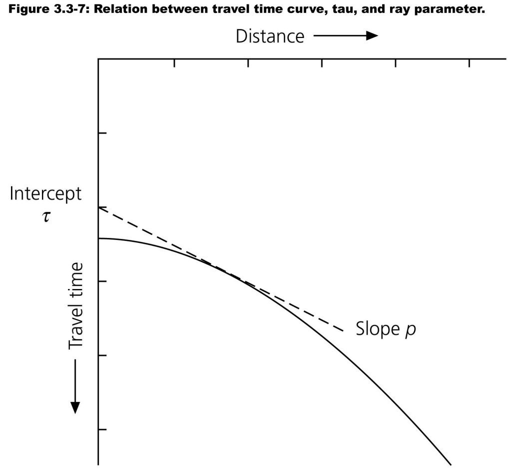

Figure 3.3-8: Relation between tau-p, and travel time curves.

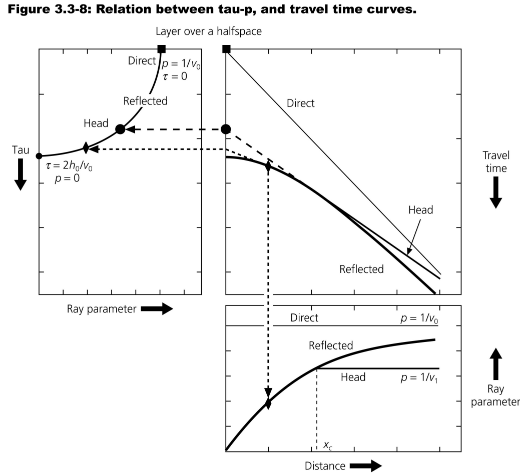

Figure 3.3-23: Illustration of slant stacking.

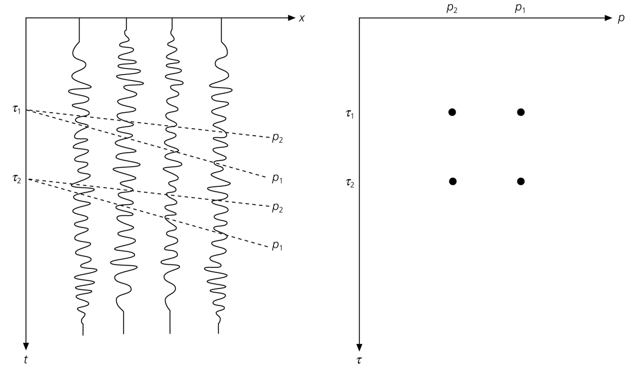

Figure 3.3-24: Example of analysis of a common source point gather of Vibroseis data.

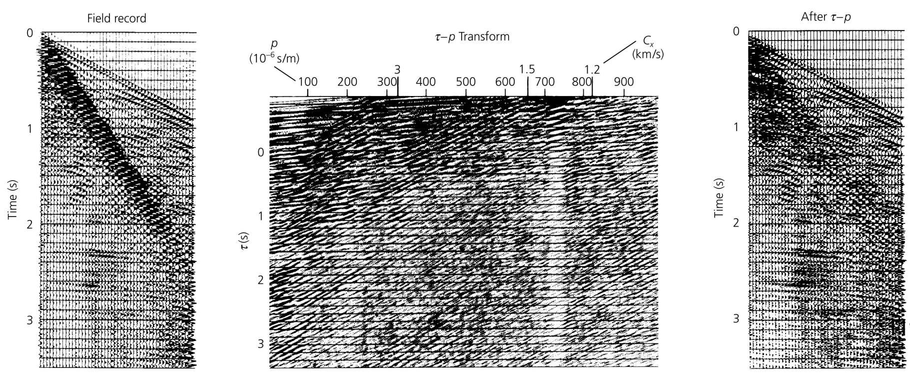

Figure 3.3-32: Three idealized seismic reflection experiments.

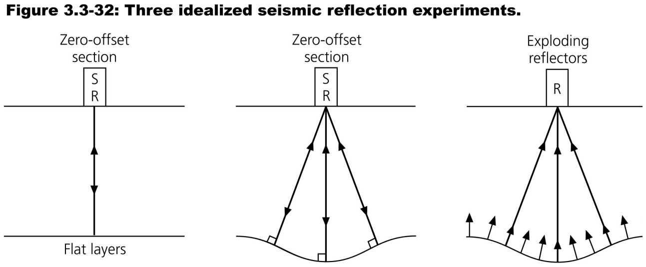

Figure 2.5-15: Huygens' generation of circular wave fronts.

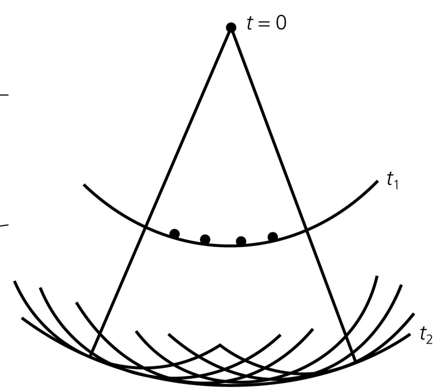

Figure 2.5-16: Huygens' principle for the propagation of a straight wave front.

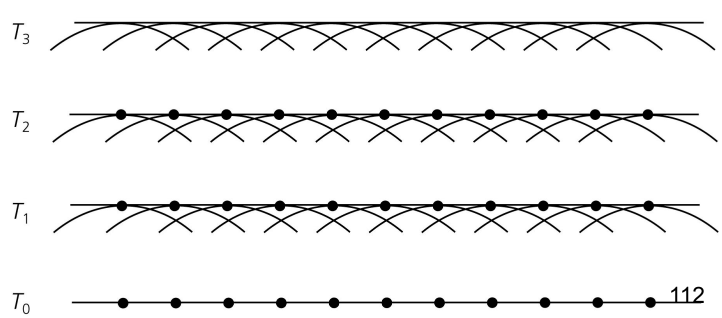

Figure 3.3-33: Effect of a point source or diffractor.

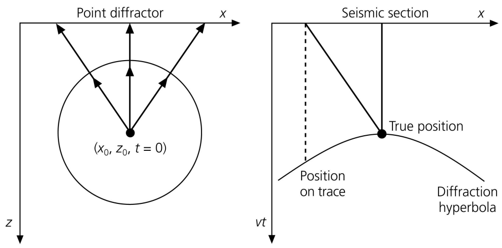

Figure 3.3-34: Diffraction hyperbola with true amplitudes.

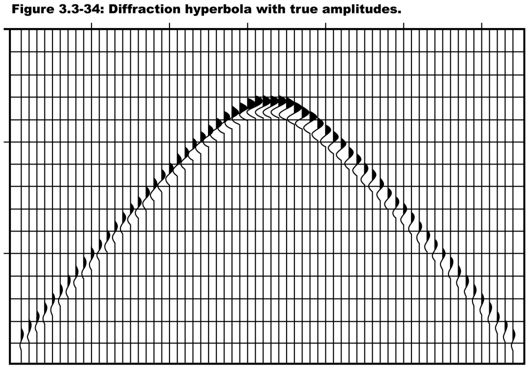

Figure 3.3-35: Modeling a dipping layer as a line of point diffractors.

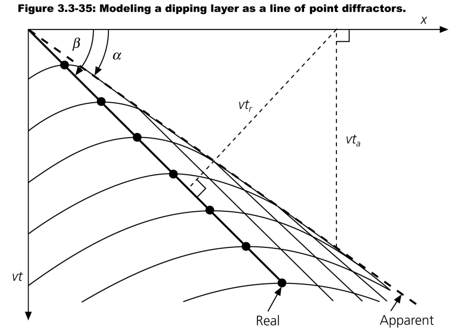

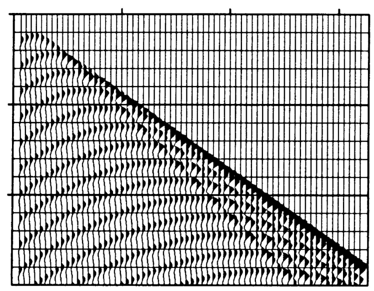

Figure 3.3-36: Generation of a "bowtie" structure.

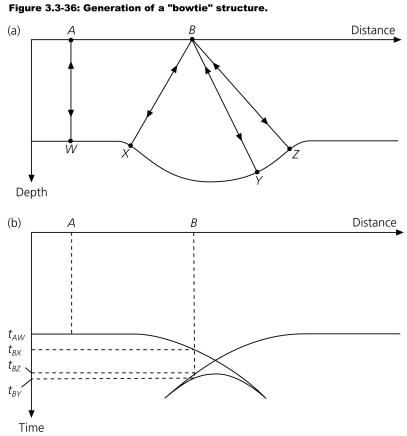

Figure 3.3-37: Diffraction off the ends of truncated interfaces.

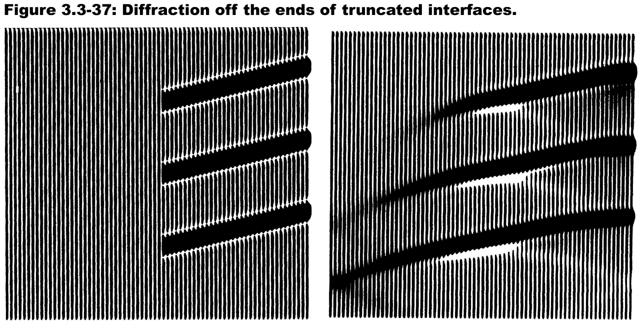

Figure 3.3-38: Illustration of Kirchoff migration.

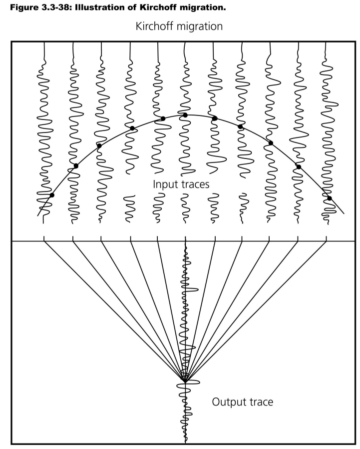

Figure 3.3-39: Time section before and after migration.

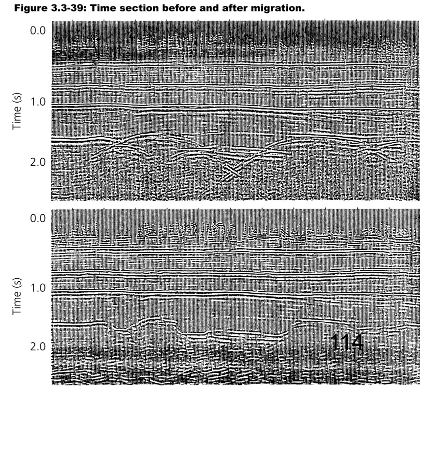

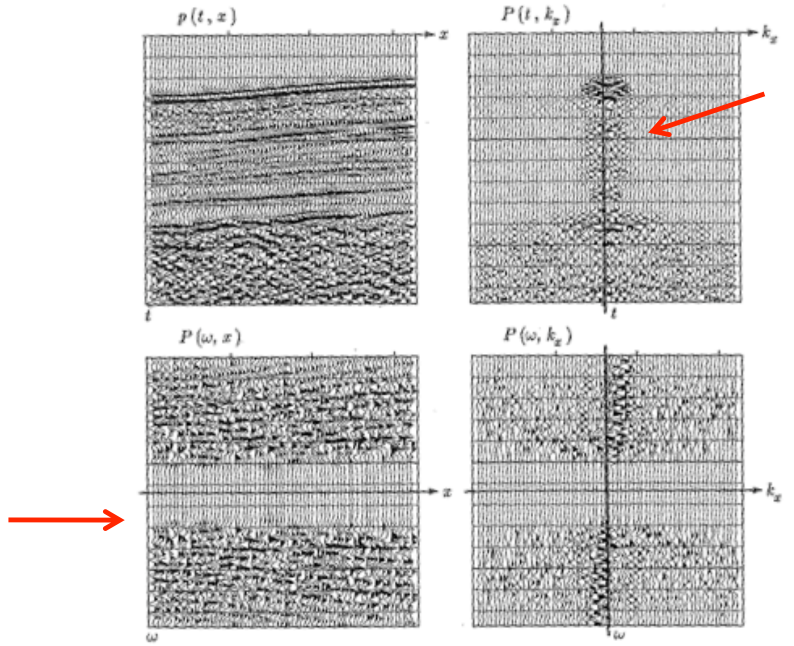

FIG. 1.2-5. A deep-marine dataset $p(t, x)$ from Alaska (U.S. Geological Survey) and the real part of various Fourier transforms of it. Because of the long travel time through the water, the time axis does not begin at $t = 0$.

Claerbout 1985

Recorded data

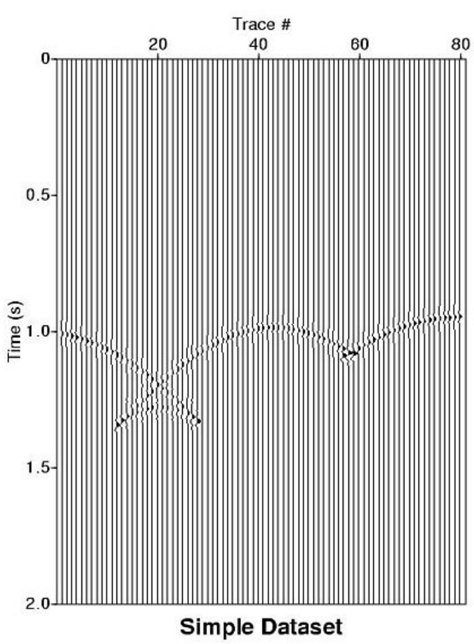

Migrated

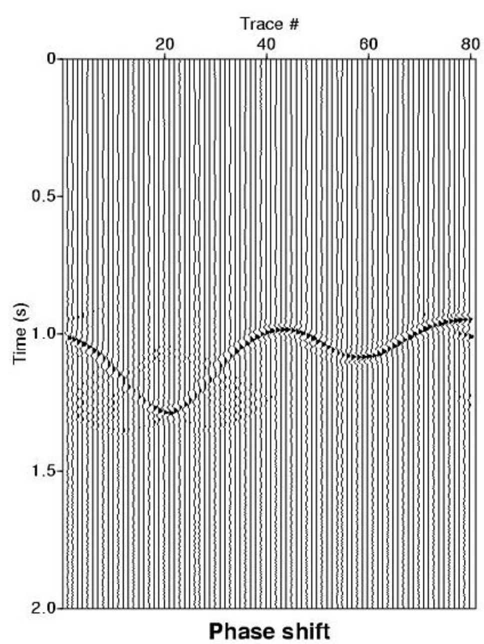

Reversed Time migration

(McMechan, 1983)

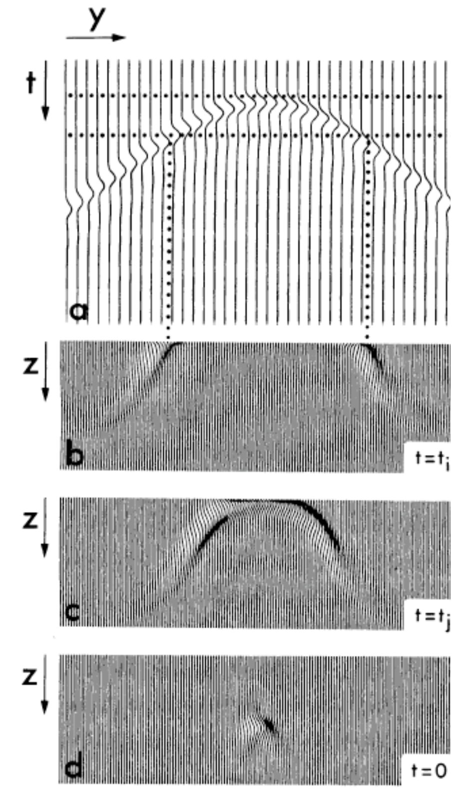

117

Guan et al, 2009

Kirchoff

RTM

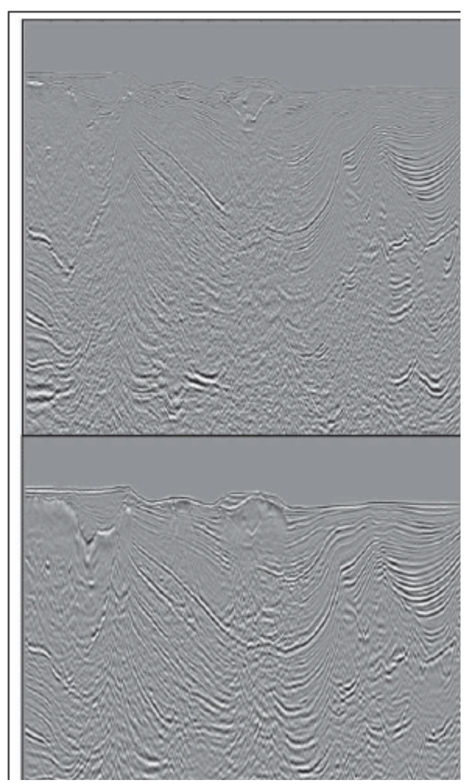

118

Figure 3.3-40: Illustration of the relation between processing operations for reflection data.

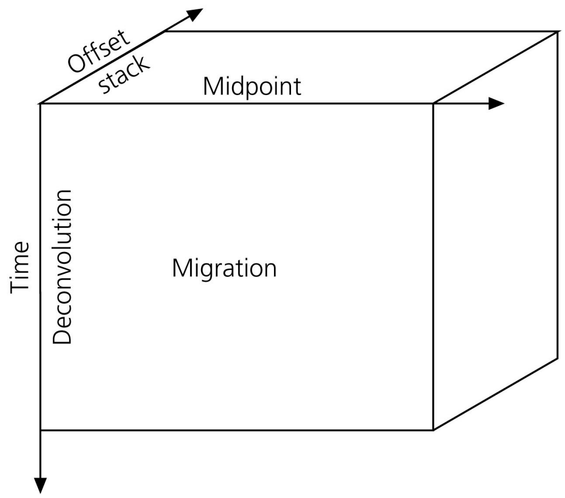

Figure 7.2-1: Geometry for earthquake location in a homogeneous halfspace.

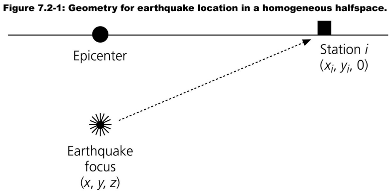

Figure 7.2-2: Illustration of the the effect of linearizing about an inverse problem starting model.

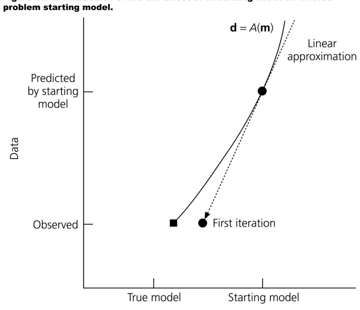

Figure 7.2-3: Illustration of the misfit to data as a function of inverse problem iteration.

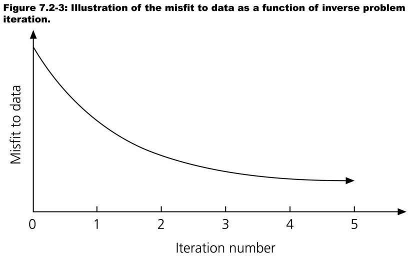

Figure 7.2-4: Map view of Cartesian relation between epicenter and station.

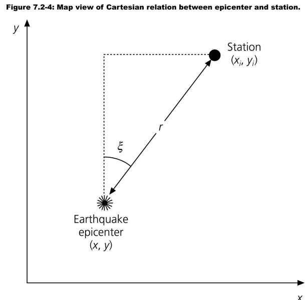

Figure 7.2-5: Example of a joint epicenter determination relocation study.

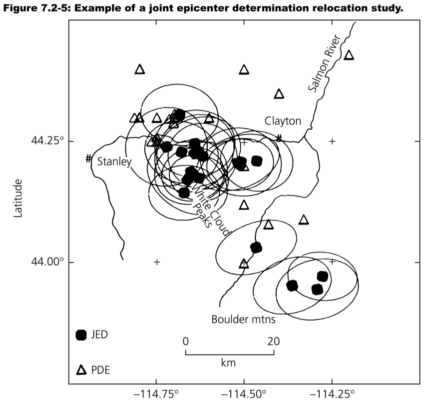

Figure 7.3-1: Geometry of a region being studied using travel time tomography.

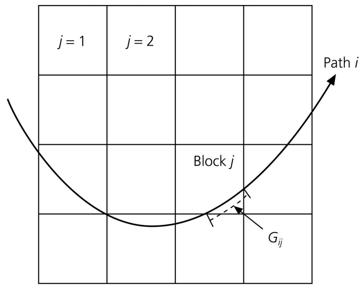

Figure 7.3-2: Ray path and block geometry for an idealized tomographic experiment.

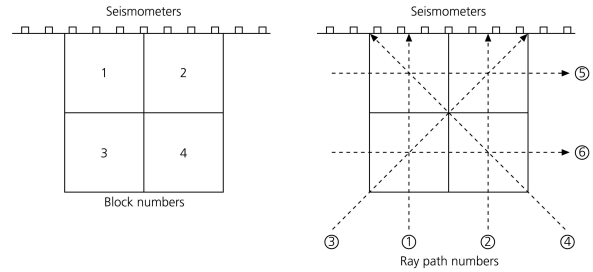

Figure 7.3-3: Illustration of "blurring" due to incomplete ray coverage.

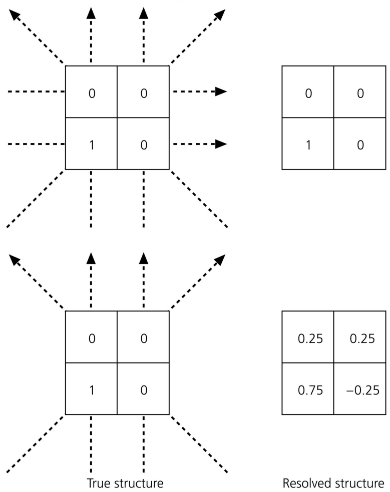

Figure 7.3-4: Illustration of the relation between the data and model spaces.

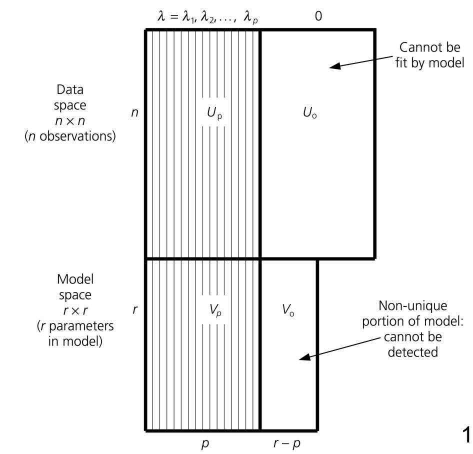

Figure 7.3-5: Example of the use of a block model for carrying out a tomographic inversion.

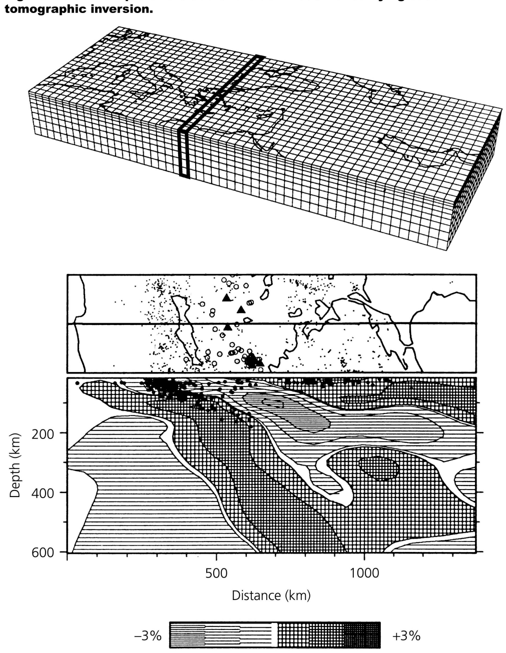

Figure 7.3-6: Example of a cell hit count and resolution test for a tomographic inversion.

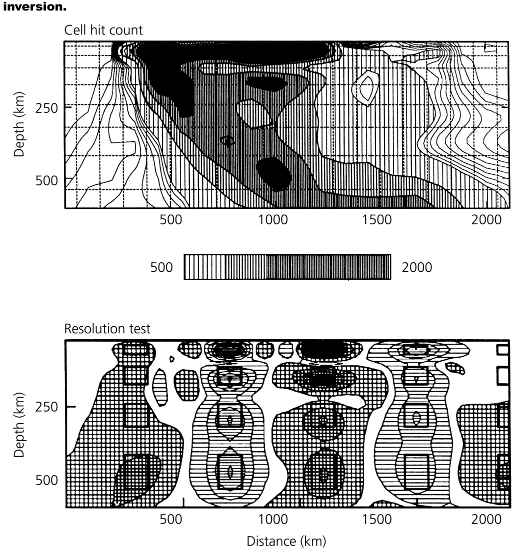

Figure 7.3-7: Example of the effects of the reference model on a tomographic inversion.

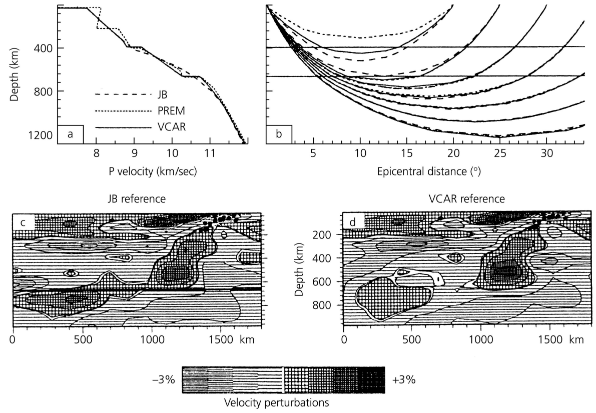

Figure 7.3-8: Example of cross-borehole tomography.

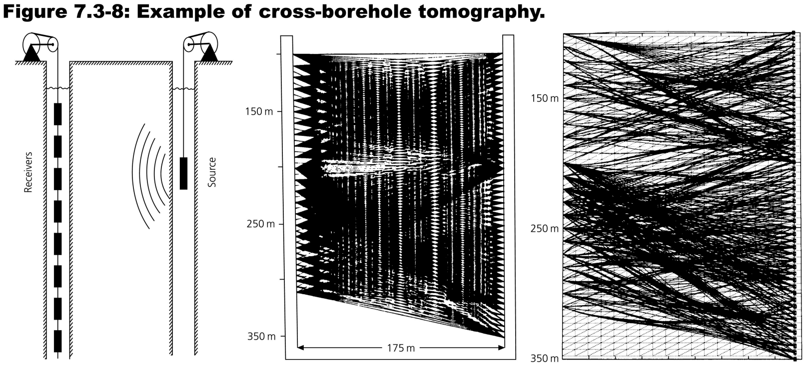

Figure 7.4-1: Relation between normal mode peak and mode attenuation.

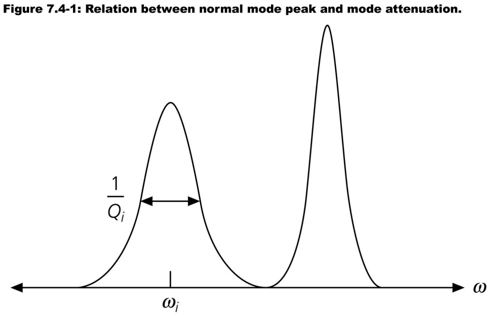

Figure 7.4-2: Example of observed attenuation for fundamental spheroidal modes.

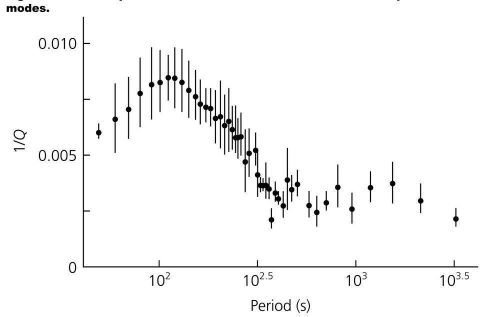

Figure 7.4-3: Examples of attenuation kernels for various modes.

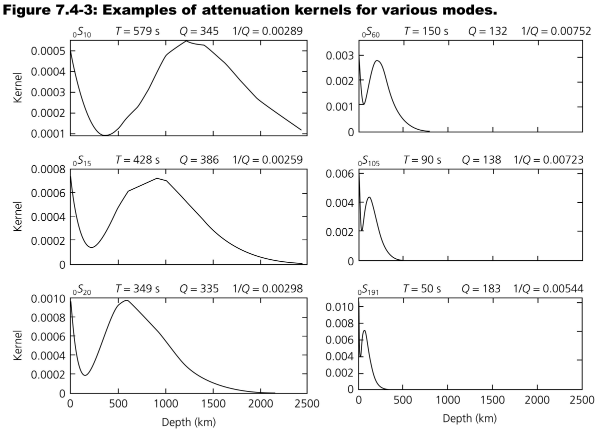

Figure 7.4-4: Illustration of model parameterizations for two types of inversion methods.

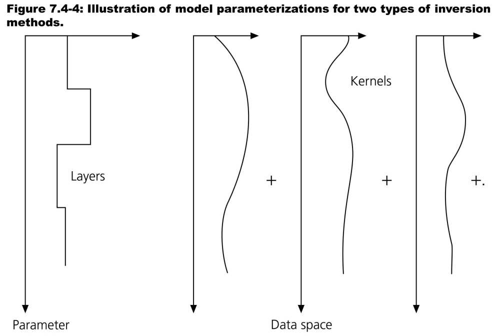

Figure 7.4-5: Example of the comparison of various attenuation models.

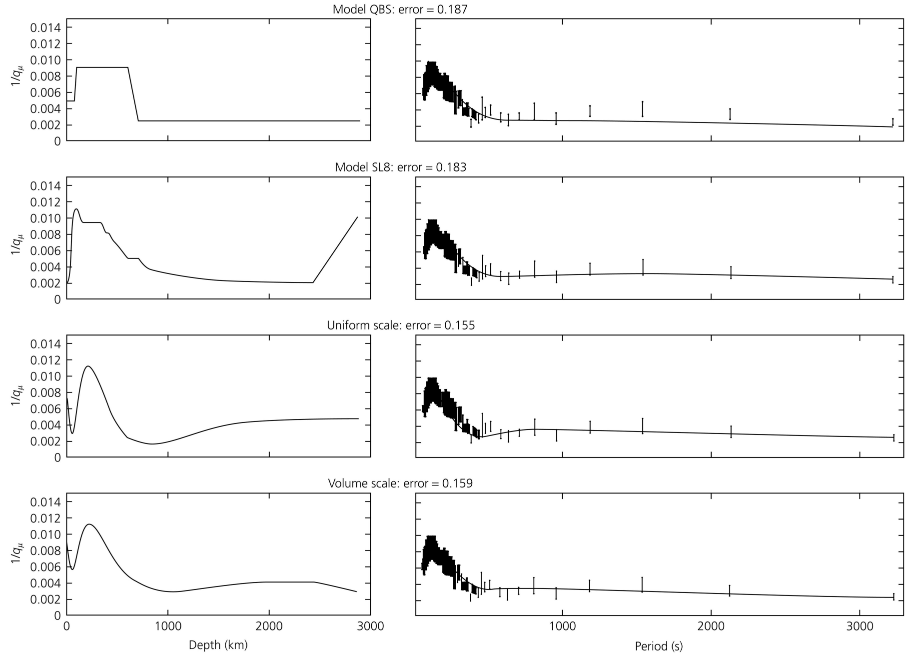

Figure 7.4-6: Example of inverting Rayleigh waves for oceanic shear wave velocity structure.

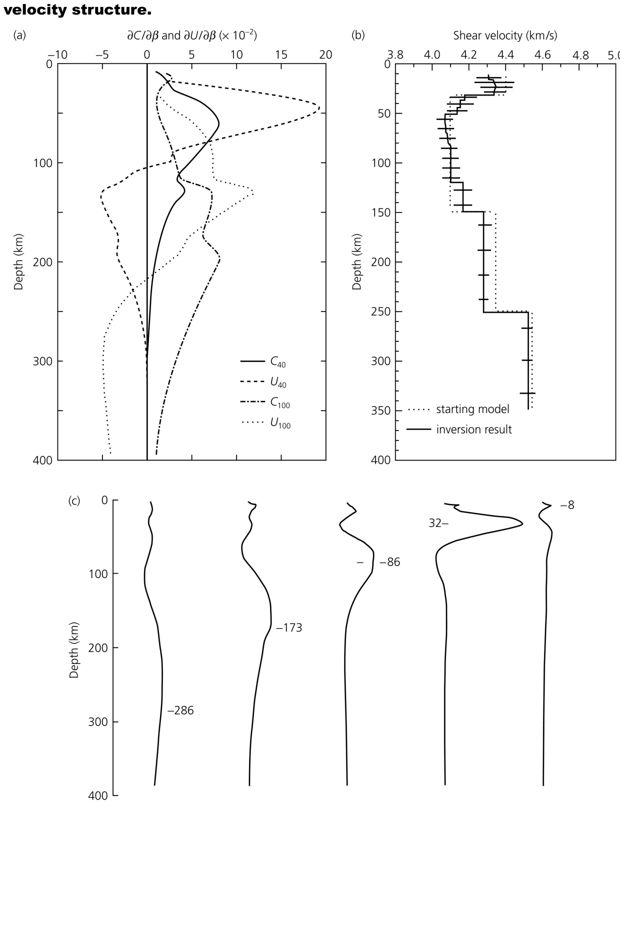

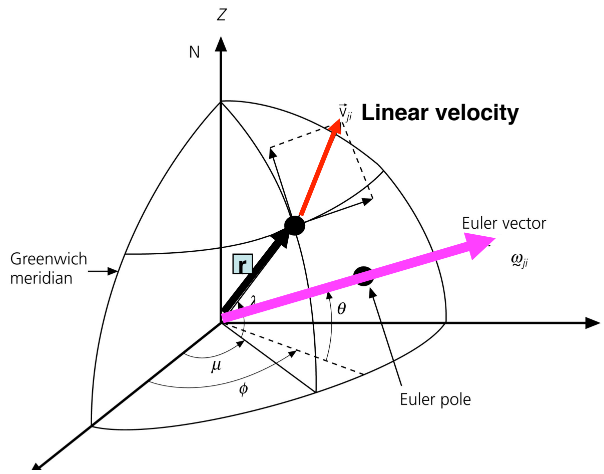

5.2-1

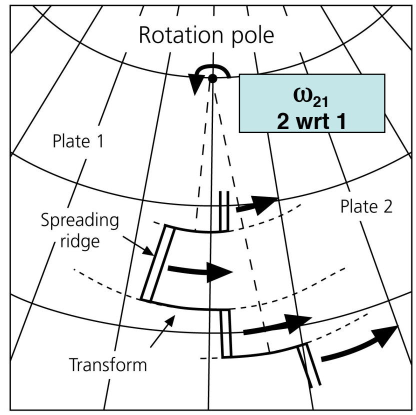

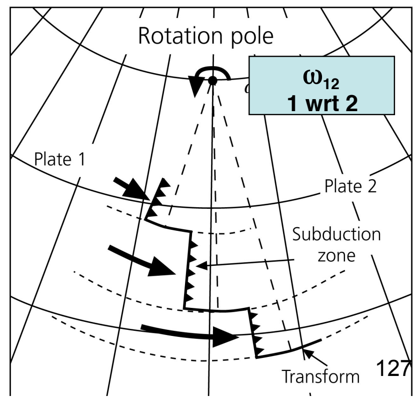

5.2-2

BOUNDARY TYPE CHANGES WITH ORIENTATION

PACIFIC - NORTH AMERICA

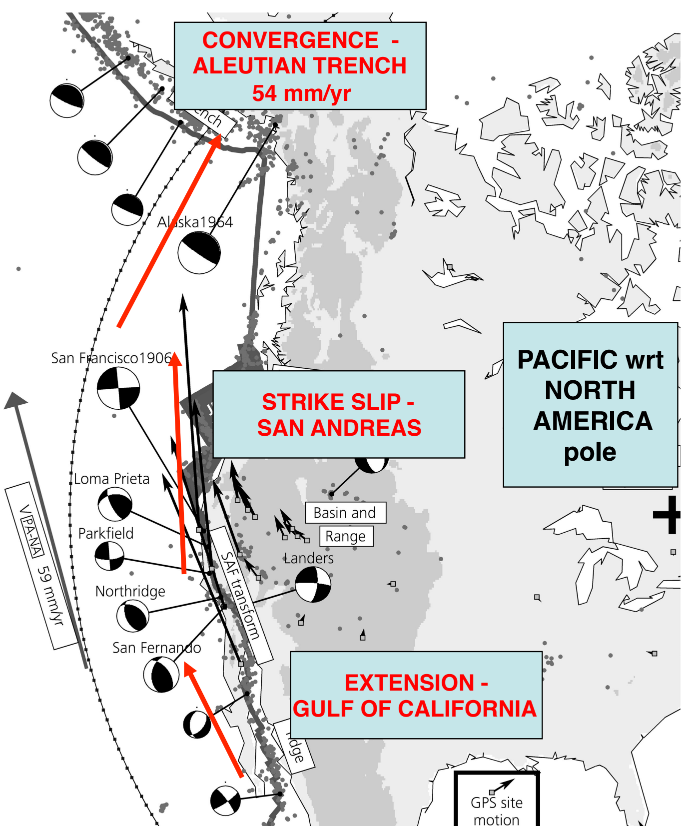

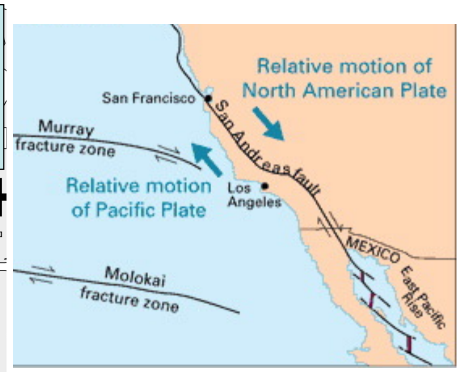

5.2-3

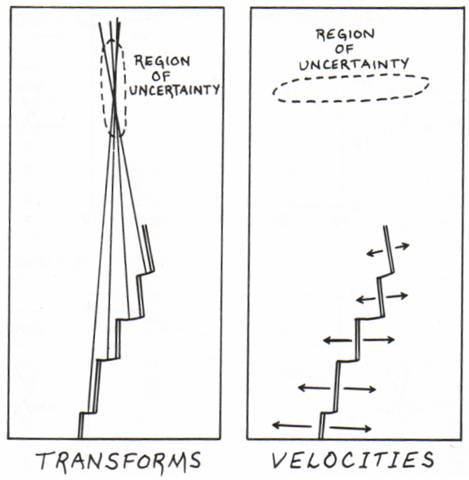

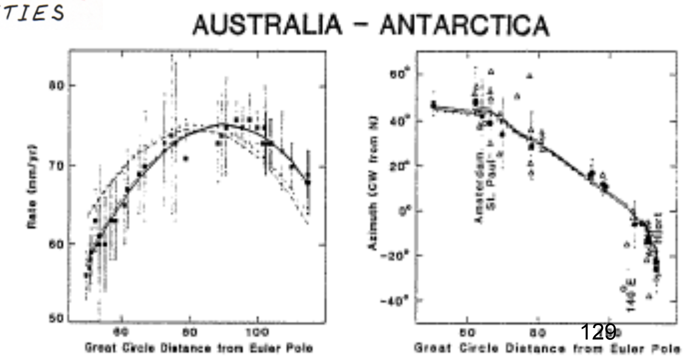

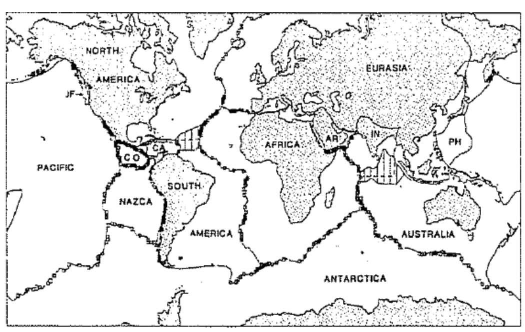

Figure 4. Data locations and plate geometry assumed for NUVEL-1. Regions with vertical lines mark diffuse plate boundaries between North and South America and between India and Australia. Within each of these diffuse boundaries a dashed line shows the discrete boundary assumed in NUVEL-1. Squares show locations of spreading rates, circles show locations of transform azimuths, and triangles show earthquake locations for slip vectors (except those along transform faults offsetting mid-ocean ridges, which are omitted for clarity). Also shown are two plates (Philippine and Juan de Fuca) omitted from NUVEL-1, but included in Table 1 for completeness. Plate name abbreviations: Cocos (CO), Caribbean (CA), Indian (IN), Arabian (AR), Philippine (PH), and Juan de Fuca (JF). Mercator projection.

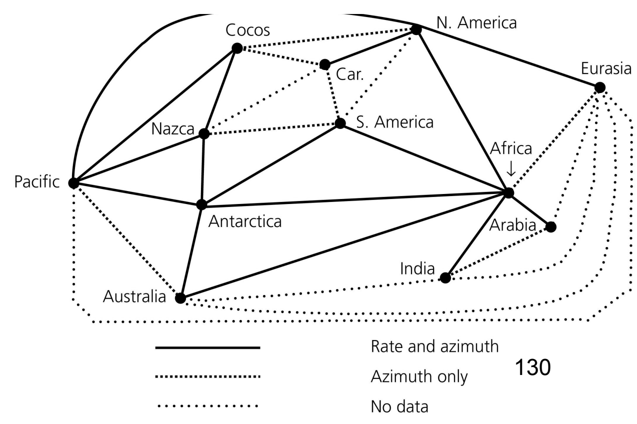

Figure 1.1-8: Inversion modeling flow chart.

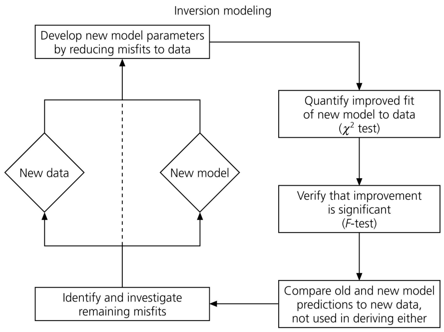

Figure 1.1-9: Evolution of successive global plate motion models.

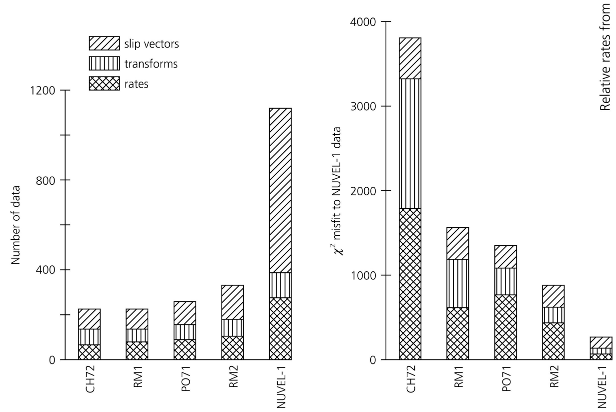

Figure 5.2-6: Correlation of current and history plate velocities.

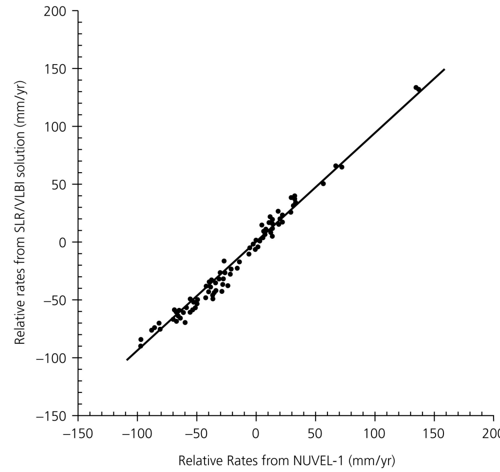

UNCERTAINTIES IN SOLUTION

Uncertainties in model vector $\sigma^2_{\mathbf{m}}$ (Euler vectors)

Derived by propagation of errors via matrix V of uncertainties in data vector d

Uncertainties in the estimated Euler vectors are given by the model variance-covariance matrix

$$\sigma^2_{\mathbf{m}} = (G^T V^{-1} G)^{-1}.$$

Uncertainties associated with Euler poles are often shown by error ellipses, whereas those for the rates are quoted separately. Two Euler vectors are distinct if their error ellipses and rates do not overlap.

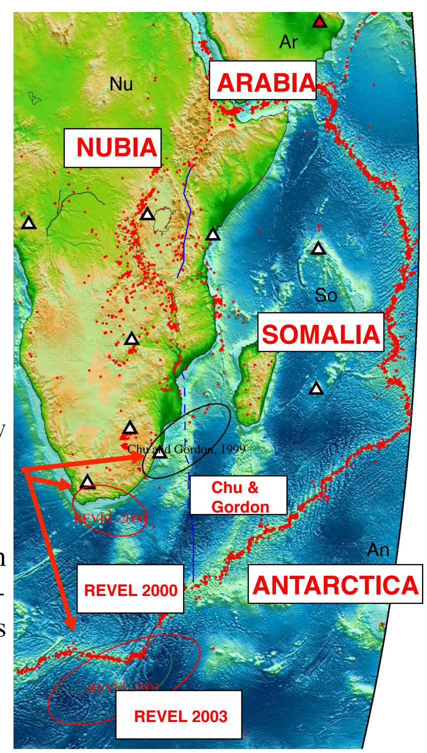

Distinct models for the motion of Nubia (West Africa) with respect to Somalia (East Africa)

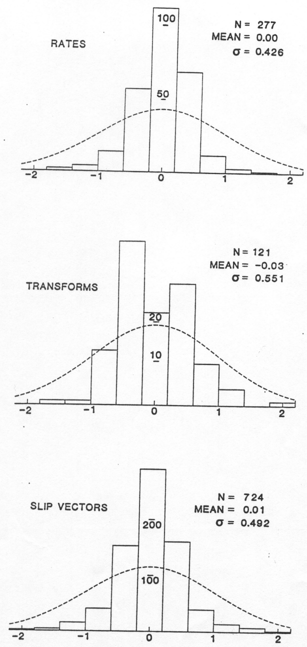

Figure 9. Histogram of the distribution of normalized errors ([Observed–Predicted]/σ) for rates, transform azimuths, and slip vector azimuths. The dashed curve shows the Gaussian distribution expected if the data uncertainties were properly estimated. The computed sample standard deviation is less than unity, showing that the data uncertainties were systematically overestimated.

Figure 7.5-1: Cumulative probability distribution.

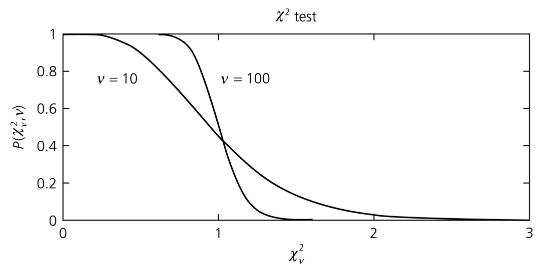

IS RIVERA DISTINCT FROM NORTH AMERICA & COCOS PLATES?

Rates & directions from transform and earthquake slip vector azimuths along presumed Pacific-Rivera boundary misfit by Pacific-North America and Pacific-Cocos motion

Improved fit from a distinct Rivera plate passes F test, so plate can be resolved